Correcting Calibrated Infrared Sky Imagery for the Effect of an Infrared Window

Paul W. Nugent, Joseph A. Shaw, and Nathan J. Pust

Electrical and Computer Engineering Department, Montana State University, Bozeman, Montana

Sabino Piazzolla

Jet Propulsion Laboratory, California Institute of Technology, Pasadena, California

ABSTRACT

A method is demonstrated for deriving a correction for the effects of an infrared window when used to weatherproof a radiometrically calibrated thermal infrared imager. The technique relies on initial calibration of two identical imagers without windows and subsequently operating the imagers side by side: one with a window and one without. An equation is presented that expresses the scene radiance in terms of through-window radiance and the transmittance, reflectance, and emissivity of the window. The window's optical properties are determined as a function of angle over the imager's field of view through a matrix inversion using images observed simultaneously with and without a window. The technique is applied to calibrated sky images from infrared cloud imager systems. Application of this window correction algorithm to data obtained months before or after the algorithm was derived leads to an improvement from 0.46 to 0.91 for the correlation coefficient between data obtained simultaneously from imagers with and without a window. Once the window correction has been determined, the windowed imager can operate independently and provide accurate measurements of sky radiance.

1. Introduction

Longwave infrared (LWIR) imagers or radiometers deployed outdoors for remote sensing measurements often require a weatherproof enclosure with an optical window or hatch to protect the instrument from precipitation or sea spray. Mechanical hatches or shutters, which require no window compensation, have been used on infrared sky imagers [Infrared Cloud Imager (ICI); Shaw et al. 2005; Thurairajah and Shaw 2005] and infrared spectroradiometers (Han et al. 1997; Minnett et al. 2001; Knuteson et al. 2004). Windows used in radiometrically calibrated systems require compensation for their optical effects. For example, the Calibrated Infrared In situ Measurement System (CIRIMS) is a shipborne infrared radiometer whose data are corrected for the effects of an intervening window using a multiparameter curve fit (Jessup et al. 2002; Jessup and Branch 2008). Another example is a multiwavelength microwave and infrared sky radiometer whose infrared channel views the sky through an infrared window. The optical effects of the window are compensated for with a combination of laboratory measurements and real-time removal of a reflection term determined with a small temperature-controlled plate located at the specular angle of the tilted window (R. Ware 2009, personal communication). The approach we describe here is better suited to applications where the LWIR sensor has a wide field of view (larger than approximately 10°).

The window correction routine presented here was developed to compensate for the optical effects of a germanium window on a compact version of the ICI system called the ICI2, which has been developed at Montana State University (MSU) in collaboration with the Jet Propulsion Laboratory (JPL). The ICI2 is a radiometrically calibrated thermal infrared imager designed to measure cloud distribution and transmittance in potential Earth–space optical communication paths (Nugent et al. 2009; Nugent 2008), which builds on the legacy of the original ICI system developed for climate studies (Shaw et al. 2005; Thurairajah and Shaw 2005). In the ICI2 system, a LWIR camera and electronics are mounted inside a weatherproof enclosure

Corresponding author address: Joseph A. Shaw, Electrical and Computer Engineering Department, Montana State University, 610 Cobleigh Hall, Bozeman, MT 59717.
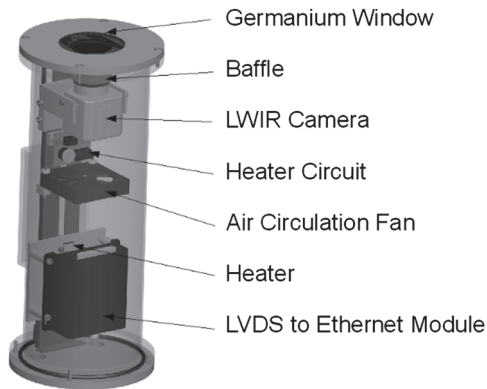E-mail: jshaw@ece.montana.edu

FIG. 1. The compact ICI2 system in its environmental enclosure, which includes a germanium window.

FIG. 2. Diagram of an IR camera behind an IR window. The signal measured by the camera depends on factors that include scene radiance L_s, window transmittance τ_w, window reflectance ρ_w, thermal emission from inside the enclosure L_e, and thermal emission from the window L_w.

(Fig. 1). Owing to size and complexity constraints, the ICI2 uses a germanium infrared window with an external hard-carbon coating to protect the instrument from precipitation, as shown in Fig. 1.

The camera used in the ICI2 is based on the FLIR Photon 320, which consists of a sensor with 324×256 pixels with noise equivalent temperature difference (NETD) of 33 mK. The version of the ICI2 discussed here has a $62°$ full-angle field of view (FOV) along the diagonal achieved with the 14.25-mm lens from FLIR (bandwidth ~8.6–13.2 μm). Replacing the FLIR lens with a custom-made 8.6-mm wide-angle lens allows for a version of the ICI2 with a $110°$ diagonal FOV (bandwidth ~8.8–13.5 μm). Details of this system and the radiometric calibration method are discussed elsewhere (Nugent et al. 2009; Nugent 2008).

The radiometrically calibrated ICI data, in conjunction with dedicated software, allow for cloud detection and classification through a two-step process. First, the atmospheric emission is removed from the radiometric sky data. The atmospheric emission is derived from models based on Moderate Resolution Atmospheric Transmission (MODTRAN) (Anderson et al. 1999) simulations of clear-sky emission for varying conditions, and are tuned to the spectral bandwidth of a given detector–lens combination (Nugent 2008; Shaw et al. 2005; Thurairajah and Shaw 2005). When available, radiosonde profiles of atmospheric temperature and humidity are used as inputs in these models. Once the atmospheric emission is removed, clouds are detected and classified by optical and physical properties based on the isolated cloud-emitted radiance (Nugent et al. 2009; Nugent 2008).

Two hindrances to the radiometric calibration had to be overcome to accomplish cloud detection with the compact ICI2 systems. First, these systems are based on a camera without a thermoelectric cooler (TEC) and the system response drifts with camera focal-plane-array
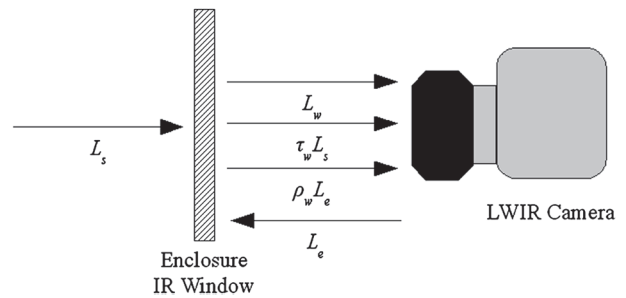
(FPA) temperature. Software routines were developed at MSU to stabilize the camera response for changes in FPA temperature using a real-time reading of the FPA temperature and laboratory-measured calibration parameters. These routines allow for a radiometric calibration to be maintained without physical temperature stabilization (Nugent 2008).

The second hindrance to calibration was the radiometric impact of the germanium window. The FPA-temperature stabilization and radiometric calibration measurements are made without the germanium window to allow the camera characteristics to be separated from the window characteristics. The addition of the germanium window limits the accuracy of these data, because the signal measured behind the window is not an accurate measure of the scene radiance. Therefore, when the system operates behind the window, the algorithms described in this paper are used to correct for the window effects in the observed data.

2. Correcting for infrared window effects

Initial tests showed that the signal from the window was not spatially uniform because of reflection of emission from the camera and warm sources located behind the camera. A shroud (or baffle) was used to block the spatially nonuniform reflections, but this shroud is still a source of emission. The measured radiance L_m is not a direct measure of scene radiance, but can be represented as a sum of scene radiance L_s multiplied by the band-averaged window transmittance τ_w, radiance emitted inside the enclosure L_e multiplied by the band-averaged window reflectance ρ_w, and radiance emitted by the window L_w, as expressed by Eq. (1) and as indicated graphically in Fig. 2. The band-averaged reflectance ρ_w is a combination of the reflectance off the bottom antireflection-coated and top hard-carbon-coated surfaces of the window, with the top surface reflection

reduced by the square of the window transmittance. However, because there was not sufficient information to isolate these two values, we derive a value of ρ_w that is effectively a combination of these terms:

$$L_m = \tau_w L_s + \rho_w L_e + L_w. \tag{1}$$

With characterization of the window, the radiance observed by a camera inside the enclosure can be corrected to yield the scene radiance that would be measured without the window. In this work, we describe a matrix-inversion technique that identifies the transmittance, reflectance, and emissivity of an infrared window averaged across the spectral response of the camera. This technique provides a method of compensating for window effects in our radiometrically calibrated infrared sky images. First, the matrix-inversion relationship is derived and explained. Next, the technique is applied to an ICI2 cloud imaging system, and the results are compared from two sets of collocated imagers in which one imager views the sky through a germanium window and the other views the sky directly.

Derivation of the window correction equation

To determine the scene radiance from a measurement taken through the window, Eq. (1) can be solved for L_s:

$$L_s = \frac{(L_m - \rho_w L_e - L_w)}{\tau_w} = \frac{1}{\tau_w}L_m - \frac{\rho_w}{\tau_w}L_e - \frac{1}{\tau_w}L_w. \tag{2}$$

The emissions from the internal enclosure L_e and the window L_w depend on the emissivity of each respective surface. If we assume that the emission from within the enclosure arises from blackbody objects at the camera temperature with emissivity equal to 1 but the band-averaged window emissivity ε_w is unknown, then the scene radiance can be expressed as

$$L_s = \frac{(L_m - \rho_w L_e - \varepsilon_w L_{w\mathrm{bb}})}{\tau_w}$$
$$= \frac{1}{\tau_w}L_m - \frac{\rho_w}{\tau_w}L_e - \frac{\varepsilon_w}{\tau_w}L_{w\mathrm{bb}}, \tag{3}$$

where $L_{w\mathrm{bb}}$ is blackbody radiance at the window temperature. If the windowless scene radiance, emission from within the enclosure, and the temperature of the window were all known, then the band-averaged properties of the window τ_w, ρ_w, and ε_w could be determined.

With these values determined, the radiative effects of the window could be removed, enabling the camera inside the enclosure to measure the scene radiance, as

measured by a camera outside the enclosure. The equation for the effective scene radiance proposed in Eq. (3) is similar to the correction used on the CIRIMS system (Jessup et al. 2002; Jessup and Branch 2008). However, for the correction derived here, there are two differences. First, our correction method is based entirely on a radiometric model of the window that allows values of τ_w, ρ_w, and ε_w to be determined in the correction procedure. Second, the cameras used in the ICI2 systems have a relatively wide FOV, and therefore our correction takes into account angular variation of the correction across the camera's FOV. We note also that this technique is based on field measurements and can therefore be applied through periodic side-by-side operation of two sky imagers to account for slow changes of window parameters over time.

3. Deriving a window correction from sky images

The window correction was developed and tested by using two identical LWIR cameras (both with 62° FOV): one operating in the enclosed system with a germanium window (the JPL-ICI2) and the other operating without a window (the MSU-ICI2). The MSU-ICI2 provided a "ground truth" measurement of the actual scene radiance L_s. Side-by-side operation of these two systems during March 2008 provided a set of data of simultaneous measurements of L_s (from MSU-ICI2) and L_m (from JPL-ICI2), the scene and measured radiances, respectively. In a previous experiment in October 2007, the JPL-ICI2 was run alongside a prototype of a 110° FOV system (110-ICI2). The 110-ICI2 system was run without a germanium window and thus allowed for a fully independent set of data, against which the window correction algorithms could be tested. The experiments used in this derivation and the following validation experiments were conducted from a rooftop deployment on the MSU campus in Bozeman, Montana.

a. Matrix-inversion technique

During this experiment, the internal emission from within the enclosure was assumed to be from the camera, and the internal temperature of the camera T_{int} was used to calculate L_e. It was also assumed that the temperature of the window largely followed the external air temperature near the enclosure T_{air}. This temperature was used to calculate the blackbody emission of an object at the window temperature $L_{w\mathrm{bb}}$. The air temperature was available from the Montana State University weather station collocated with the two cloud imagers during the experiment. These values were used to create a matrix,
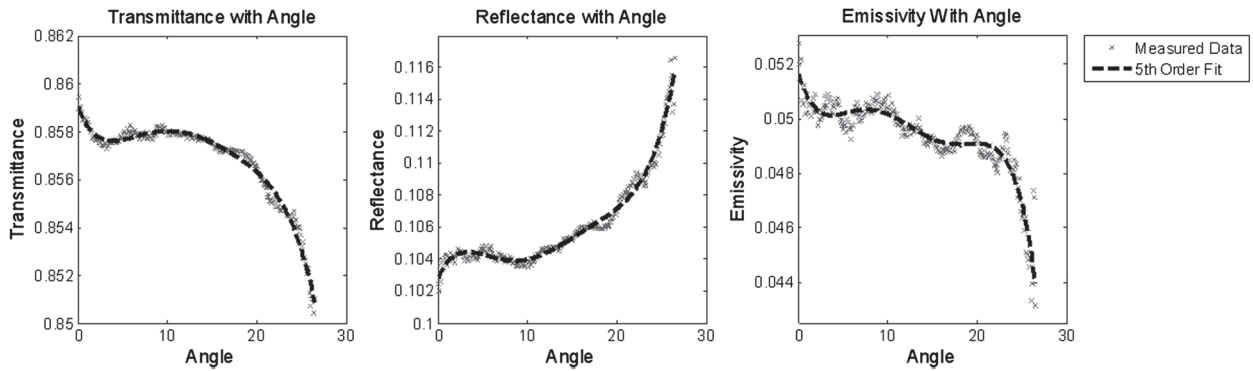
FIG. 3. (left) Transmittance, (middle) reflectance, and (right) emissivity of the IR window plotted as functions of angle. The transmittance varies from 0.850 to 0.859, with an average over all angles of 0.857. The on-axis value is close to the value of 0.90 measured for the new window with an FTIR spectrometer. The reflectance varies from 0.102 to 0.116, with an average over all angles of 0.106. The emissivity varies from 0.043 to 0.053, with an average over all angles of 0.050.

$$
\begin{bmatrix} L_{s1} \\ L_{s2} \\ L_{s3} \\ L_{s4} \\ \cdots \end{bmatrix} = \begin{bmatrix} L_{m1} & -L(T_{\text{int1}}) & -L(T_{\text{air1}}) \\ L_{m2} & -L(T_{\text{int2}}) & -L(T_{\text{air2}}) \\ L_{m3} & -L(T_{\text{int3}}) & -L(T_{\text{air3}}) \\ \cdots & \cdots & \cdots \end{bmatrix} \begin{bmatrix} \dfrac{1}{\tau_w} \\ \dfrac{\rho_w}{\tau_w} \\ \dfrac{\varepsilon_w}{\tau_w} \end{bmatrix}. \tag{4}
$$

These data were loaded into software routines that calculated the Moore–Penrose pseudoinverse matrix as indicated by the following:

$$
\begin{bmatrix} \dfrac{1}{\tau_w} \\ \dfrac{\rho_w}{\tau_w} \\ \dfrac{\varepsilon_w}{\tau_w} \end{bmatrix} = \begin{bmatrix} L_{m1} & -L(T_{\text{int1}}) & -L(T_{\text{air1}}) \\ L_{m2} & -L(T_{\text{int2}}) & -L(T_{\text{air2}}) \\ L_{m3} & -L(T_{\text{int3}}) & -L(T_{\text{air3}}) \\ \cdots & \cdots & \cdots \end{bmatrix}^{+} \begin{bmatrix} L_{s1} \\ L_{s2} \\ L_{s3} \\ L_{s4} \\ \cdots \end{bmatrix}. \tag{5}
$$

Multiplying the inverted matrix by the set of MSU-ICI2-measured external radiance L_s allows the calculation of the variables in Eq. (3). The window band-averaged transmittance τ_w is found as 1 over the first element of the resulting vector. Multiplying the other two elements of this vector by τ_w yields estimated values of ρ_w and ε_w, the window band-averaged reflectance and emissivity, respectively. For accurate characterization of these parameters, the datasets needed to contain the range of T_{int} and T_{air}, over which the imager was expected to operate. These temperatures ranged from 10° to 32°C for T_{int} and from 6° to 21°C for T_{air}, with a range of T_{int}–T_{air} from 2° to 12°C.

b. Angle-dependent IR window correction

The physical properties of the window τ_w, ρ_w, and ε_w vary with angle throughout the camera's field of view. This could be ignored in a narrow field-of-view system or a nonimaging system; however, because the ICI2 systems are relatively wide-angle imagers with incidence angles on the window up to 31°, the angular dependence cannot be ignored. For the LWIR cameras used in the ICI2 systems the per-pixel pointing angle had previously been measured (Nugent 2008). This allowed for the coefficients τ_w, ρ_w, and ε_w to be measured uniquely for each pixel and represented as functions of angles $\tau_w(\theta)$, $\rho_w(\theta)$, and $\varepsilon_w(\theta)$, where θ is the pointing angle of each pixel measured from the optical axis.

The values of $\tau_w(\theta)$, $\rho_w(\theta)$, and $\varepsilon_w(\theta)$ do not follow a simple physical model based on Fresnel reflection equations. This is in part because of the action of the carbon coating on the external window surface, antireflection coating on the inside surface, and dust and other contaminants that can settle on the window over time. Although, with sufficient information, it may be possible to develop a physical model to predict the angle-dependent parameters of the window, it is more practical to directly measure these parameters in the laboratory or to infer them from field measurements using an imager with a window alongside a system without a window. We adopted the latter approach and chose to express the angle dependence of the matrix-inversion results with a fifth-order polynomial fit to each parameter as a function of angle. To reduce measurement variations caused by pixel-to-pixel noise, the data were averaged into angle bins of width $\Delta\theta = 0.1°$. Figure 3 shows the angle-binned data and the corresponding fifth-order polynomial fits to $\tau_w(\theta)$, $\rho_w(\theta)$, and $\varepsilon_w(\theta)$.

During the experiments, both systems were pointed nominally at the zenith; however, a misalignment of approximately 1° from vertical and 2° in azimuth existed. To accommodate this problem, the data were processed to align the images, which required that the data near the edge of each camera's FOV be left out of the final result.

Thus, Fig. 3 shows plots of $\tau_w(\theta)$, $\rho_w(\theta)$, and $\varepsilon_w(\theta)$ only out to an angle of 26.6°. The transmittance for the window was observed to vary from 0.859 on axis to 0.850 at 26.6°. This on-axis value is close to the Fourier transform infrared (FTIR) spectrometer measurement of 0.90 that was made when the window was new. At the time of the measurements described in this work, the window had been deployed outside for a period of months, and some degradation was expected.

To validate our results, one should consider that, for a material in thermal equilibrium, the sum of the transmittance, reflectance, and emissivity for each angle θ must be

$$\tau_w(\theta) + \rho_w(\theta) + \varepsilon_w(\theta) = 1. \qquad (6)$$

Experimentally, we found that the mean value of τ_w, ρ_w, and ε_w measurements over the observed angles was instead 1.012, with a standard deviation of 4.1×10^{-4}. The mean value calculated from the sum of the polynomials used to fit these data was again 1.012, and the standard deviation was 3.6×10^{-4}. This sum is then close to the expected quantity of 1 at all angles, with a mean bias of ~1.2% high. This summation adds support to the reliability of this method for retrieving the window optical properties. Possible sources of the error in this summation are the uncertainty in the enclosure temperature, the window temperature, the emissivity of the enclosure interior, and the camera calibration. Whereas a 10°C error in the window temperature could account for the entire 1.2% error (a 20% error in ε_w), the source is most likely a combination of these uncertainties.

Using the empirical models for $\tau_w(\theta)$, $\rho_w(\theta)$, or $\varepsilon_w(\theta)$ with the measured pointing angle for each pixel, a unique τ_w, ρ_w, and ε_w can be calculated for each pixel of the imager. Using these calculated values with the radiance measured inside the enclosure L_m, the external scene radiance L_s can be calculated from the following equation, thereby providing a method to remove the effect of the IR window on the measured radiance values:

$$L_s = \frac{[L_m - \rho_w(\theta)L(T_{\mathrm{int}}) - \varepsilon_w(\theta)L(T_{\mathrm{air}})]}{\tau_w(\theta)}. \qquad (7)$$

4. Validation of the window correction with independent sky imagers

The window correction algorithm was validated by applying it to infrared sky images and comparing the results to measurements from a similar system operating without a window. This was done using data from two separate outdoor deployments. The first set to be ana-

lyzed was obtained in April 2008, five weeks after the measurements from which the correction was derived. During this experiment, the JPL-ICI2 (62° FOV) weatherproof system with an infrared window was operated next to the MSU-ICI2 (62° FOV) system without a window. The second dataset was obtained in October 2007, more than five months before the measurements from which the IR window correction algorithm was derived. During this earlier experiment, the JPL-IC2 (62° FOV) weatherproof system was operated next to the 110-ICI2, with 110° FOV, which operated without a window. This second set of data was used to provide a comparison independent of the instrument used to derive the window correction.

For each of these datasets, the data measured by the JPL-ICI2 with the IR window were corrected using Eq. (7), the fifth-order polynomial model of window properties, and the measured pointing angle of each pixel. It is also important to note that these validation experiments compare window-corrected data with no-window data from two totally different imagers, the MSU-ICI2 and the 110-ICI2.

The sky measurements used in these comparisons were processed to provide both cloud presence and cloud type. This cloud classification scheme is based on the dependence of cloud emission on cloud emissivity and temperature and on the strong dependence of cloud emissivity on cloud thickness for thin clouds (Nugent et al. 2009; Sassen and Mace 2002). The cloud classification scheme used to process these data is shown in Table 1. The table also lists cloud optical depth, which is commonly used to classify thin clouds, particularly cirrus. The optical depth represents the total extinction of the cloud and is also related directly to the total optical loss for a signal (e.g., sunlight or a laser) transmitted through the cloud. The visible-wavelength cloud optical depth is derived from the measured thermal emission for cirrus clouds (Nugent et al. 2009). Clouds with an optical depth above 3 act as blackbodies, and the cloud emission no longer depends on cloud thickness but rather on cloud temperature (Sassen and Mace 2002).

a. Validation with temporal cloud cover data

This section presents the temporal cloud cover data measured across the full 62° FOV of the two infrared cloud imager systems. For these time series, the data have been plotted against local time, which during these experiments was mountain daylight time (MDT = UTC − 6 h).

1) APRIL 2008 DATA

The April 2008 experiment used the same two 62° FOV cameras, calibrations, and configurations that were

TABLE 1. Cloud type and optical depth classification thresholds.

Cloud classification	Max cloud optical depth at 550 nm	Max cloud loss (dB) at 550 nm	110-ICI2 (110° FOV) threshold (W m^{-2} sr^{-1})	JPL-ICI2, MSU-ICI2 (62° FOV) thresholds (W m^{-2} sr^{-1})
Undetectable	<0.15	<0.65	<1	<1
1	<0.25	<1.09	1–1.8	1–2.0
2	<1	<4.34	1.8–3.6	2–4
3	<3	<13.02	3.6–5.5	4–6
4	Mixed	>13.02	5.5–8	6–9
5	High	High	8–12	9–13
6	High	High	12–20	13–22
7	High	High	>20	>22

used to develop the window correction. The MSU-ICI2 system ran without a window, whereas the JPL-ICI2 ran inside its enclosure with the germanium window in place. These data were taken more than a month after the data from which the correction was derived, and represent an independent set of data. Figure 4 shows the spatially averaged atmospheric radiance measured by each system as a function of time on 29 April 2008. The data for the JPL 62° FOV system are presented both before and after the correction in Eq. (7) was applied.

Application of the IR window correction significantly reduced the differences between the data from these two systems. The rms difference was 4.9 W m^{-2} sr^{-1} before the correction was applied and 0.77 W m^{-2} sr^{-1} after the correction was applied. This residual error may be reduced even further by using a temperature sensor mounted on the window rather than on a weather station located 10 m away, as was done here.

2) OCTOBER 2007 DATA

Data obtained during an experiment in October 2007 provide an independent comparison with a cloud imager based on the same sensor but with a different lens, FOV, and spectral transmittance function. During this experiment, the JPL-ICI2 (62° FOV) ran beside the prototype 110-ICI2 (110° FOV) system with no window. Only data within the overlapping center 62° (diagonal FOV) of the 110° FOV system were used in the comparison. Furthermore, because the optical bandwidths of these cameras are different, the radiance measured by each camera when viewing identical scenes was different. Therefore, in this section, processed cloud amount is used as the basis of comparison. The cloud detection thresholds (Table 1) and atmospheric correction algorithms are adjusted to each camera's bandwidth to remove the bandwidth-dependent bias between the two systems (Nugent 2008).

Figure 5 shows the amount of thin cloud (types 1–3 in Table 1) detected over the center 62° FOV of the 110-ICI2 and the full 62° FOV of the JPL-ICI2, before and after the window correction algorithm was applied to data measured on 2 October 2007 (the sensors did not operate from 1600 to 1745 MDT on this day because of precipitation). The Pearson product–moment correlation
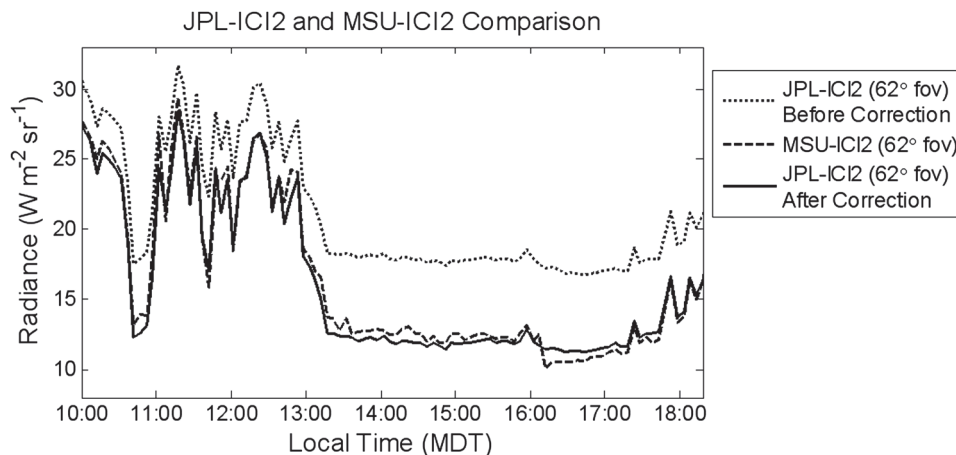

FIG. 4. Atmospheric radiance averaged over the full FOV of the MSU-ICI2 with 62° FOV and JPL-ICI2 with 62° FOV cloud imagers on 29 Apr 2008. Applying the IR window correction reduces the rms difference from 4.9 to 0.77 W m^{-2} sr^{-1}.
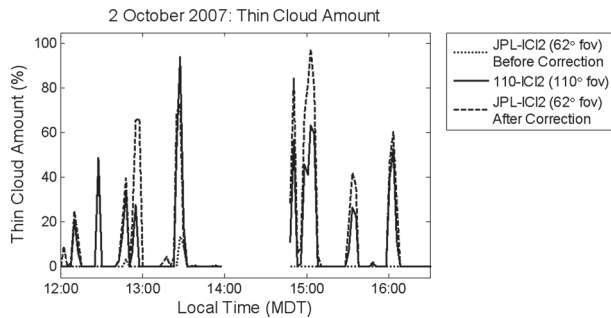
2 October 2007: Thin Cloud Amount

FIG. 5. Thin cloud amount derived from side-by-side imagers on 2 Oct 2007. With the germanium window in place, and before the window correction is applied, the cloud amounts from the two systems have a correlation coefficient of 0.46; applying the window correction improves the correlation to 0.91. This is close to the correlation of 0.96 that is achieved on subsequent days, when the window was not present on either system.

coefficient between the cloud data before the correction was 0.46, but improved to 0.91 after the correction was applied. During the subsequent days of the experiment, with cloud data obtained with the two side-by-side imagers—both operating without a window—the correlation was 0.96. Thus, the correlation for the window-corrected data was slightly less than when the IR window was not present, but represents a significant improvement in the data measured through the window.

b. Spatial cloud detection validation

In this section, we compare spatial cloud maps generated by the ICI2 systems with and without window correction to demonstrate that the correction has accurately taken into account the angular dependence of the correction coefficients. With the correction applied, the two systems see nearly identical spatial cloud statistics, with little to no field-of-view-dependent variation.

1) 29 APRIL 2008

Figures 6 and 7 show images obtained at 1137 MDT 29 April 2008, when the MSU-ICI2 system was run alongside the JPL-ICI2 system. The panels of Fig. 6 show the uncorrected cloud map measured by the JPL-ICI2 system viewing the sky through the IR window (left), the cloud map measured by the MSU-ICI2 system with no window (middle), and the window-corrected cloud map for the JPL-ICI2 62° FOV system (right). Figure 7 shows difference images between these two systems before (left) and after correction (right).

2) 2 OCTOBER 2007

In Figs. 8 and 9, we present data from 2101 MDT 2 October 2007, when the JPL-ICI2 system with a window was run alongside the 110-ICI2 with no window. The cloud data are presented in the same manner as the

April 2008 data, except that in these comparisons only the center 62° of the 110° FOV was used and the 62° data were downsampled through interpolation to match the resolution of the center 62° of the 110° imager. The image panels in Fig. 8 show the uncorrected cloud map measured by the JPL-ICI2 system through an IR window (left), the cloud map measured by the 110-ICI2 system (middle), and the corrected cloud map for the JPL-ICI2 62° system (right). The image panels in Fig. 9 show the difference image between the 110-ICI2 and the JPL-ICI2 before (left) and after (right) correction for the window.

c. Results of the validation

Both the temporal and the spatial cloud data demonstrate that the window correction greatly reduces the differences between simultaneous cloud data measured with different imaging systems. When the time series plots of spatially averaged radiance from the two 62° FOV systems were compared (see Fig. 4), the window correction reduced the rms differences from 4.9 to 0.77 W m^{-2} sr^{-1}. For comparison, the calibration accuracy of ICI2 systems has been determined to be near ± 0.45 W m^{-2} sr^{-1} without the window (Nugent 2008). Therefore, the expected variation between the two imagers resulting from calibration uncertainty was ± 0.63 W m^{-2} sr^{-1} (Nugent 2008). In the spatial data, the only persistent differences between the 62° JPL system and the other systems occurred near the cloud borders, which are highly sensitive to any angular misalignment between the two cameras. Differences observed in both temporal and spatial data were small enough to be generally lower than the cloud identification threshold radiance values.

An additional benefit of this comparison is that the rms deviation between the two imager signals can be used to estimate the calibration uncertainty of the windowed imager after correction for the window effect. We follow Bevington's treatment of propagation of errors (Bevington 1969), which says that the variances add for independent data, as indicated in the following:

$$\sigma_x^2 = \sigma_a^2 + \sigma_b^2, \tag{8}$$

where σ_x represents the standard deviation of the difference between the window-corrected signal from the JPL-ICI2 and the windowless MSU-ICI2, σ_a represents the calibration uncertainty of the windowless MSU-ICI2, and σ_b represents the calibration uncertainty of the windowed JPL-ICI2 after window correction. We can then obtain an estimate of the calibration uncertainty of the window-corrected JPL-ICI2 by solving Eq. (8) for σ_b:

Uncorrected JPL-ICI2 62° data   MSU-ICI2 62° data   Corrected JPL-ICI2 62° data

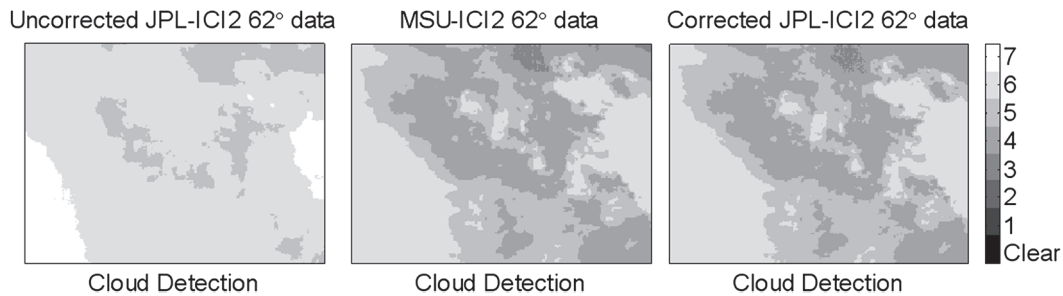Cloud Detection   Cloud Detection   Cloud Detection

FIG. 6. Cloud detection images from two cloud imagers taken at 1137 MDT 29 Apr 2008. The image panels show cloud maps from (left) the uncorrected JPL-ICI2 62° system with the IR window, (middle) the MSU-ICI2 62° system with no window, and (right) the corrected JPL-ICI2 62° system. The grayscale bar represents the cloud classification bins from Table 1.

$$\sigma_b = \sqrt{\sigma_x^2 - \sigma_a^2}. \qquad (9)$$

Applying this equation to the measured data leads to an uncertainty of ± 0.64 W m^{-2} sr^{-1} for the window-corrected JPL-ICI2. This uncertainty is higher than the value of ± 0.45 W m^{-2} sr^{-1} that was calculated for a windowless ICI2, and it therefore limits the JPL-ICI2 to a minimum threshold of level-2 clouds (see Table 1) for accurate cloud detection and classification. Thus, when this system is run with its germanium IR window, it can accurately classify clouds with a 550-nm optical depth greater than 0.25 (see Table 1), which includes all but the thinnest clouds.

This level of sensitivity is sufficient for an infrared cloud imaging system in many applications. For example, in an Earth–space optical communication system, this level corresponds to a cloud-dependent loss of approximately 1 dB, which is likely to be acceptable for Earth–space communication links with near-Earth

platforms. It has also been suggested that a sensitivity threshold of 0.25 for cloud optical depth provides the best fit with traditional cloud climatology (performed by human observers), in particular when used as a detection threshold for lidar-based systems in the Arctic (Eloranta et al. 2008). Thus, the ICI2, when operating in the enclosure and behind the germanium window, can provide the required accuracy and sensitivity needed for cloud cover studies with consistent day and night detection. Operation without a window can produce better sensitivity, but it is at the expense of somewhat increased mechanical complexity through the use of a remotely operated protective hatch.

5. Conclusions

We have described a technique based on field measurements to determine the transmittance, reflectance, and emissivity of an infrared window, including angular dependence over a moderately wide-angle image. This

Uncorrected Difference   Corrected Difference
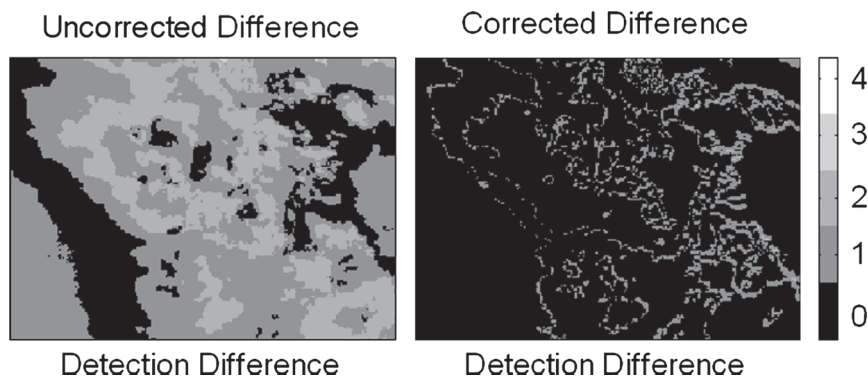
Detection Difference   Detection Difference

FIG. 7. Difference of cloud detection images from the two side-by-side cloud imagers for 1137 MDT 29 Apr 2008 (left) before and (right) after correction. The grayscale bar indicates the magnitude of the error in terms of the number of cloud classification bins from Table 1. The IR window correction greatly reduces the differences to only one cloud classification bin at the cloud edges because of slight misalignments between the imagers and small calibration differences.

Uncorrected JPL-ICI2 62° data   110-ICI2 (Center 62°) data   Corrected JPL-ICI2 62° data

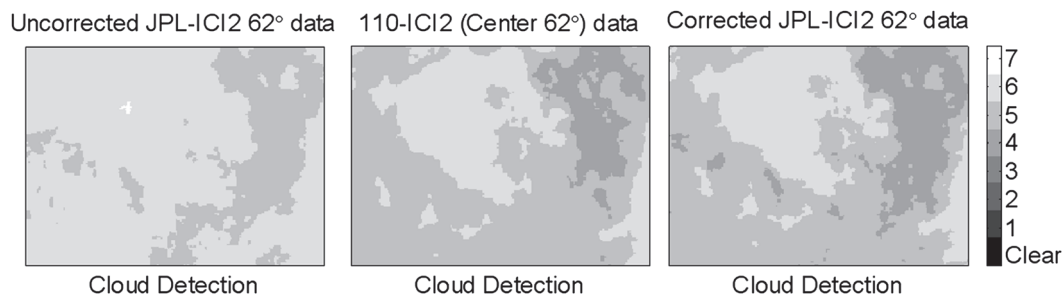Cloud Detection   Cloud Detection   Cloud Detection

FIG. 8. Cloud data from two cloud imagers taken at 1906 MDT 2 Oct 2007. The image panels show cloud maps from (left) the uncorrected JPL-ICI2 62° system, (middle) the center 62° of the 110-ICI2 110° system, and (right) the corrected JPL-ICI2 62° system. The grayscale bar represents the cloud classification bins from Table 1.

technique produces a correction for thermal infrared imagery taken through a germanium window and requires data from two collocated thermal infrared cameras, internal camera temperature, and external air temperature. This technique has been applied successfully to measure the LWIR band-averaged transmittance τ_w, reflectance ρ_w, and emissivity ε_w of a germanium IR window in a thermal infrared camera enclosure over a 62° FOV.

With this correction applied, the signal measured by the camera behind the IR window can be corrected to represent the true scene radiance to within ±0.64 W m^{-2} sr^{-1}. Through the application of this correction, the weatherproof JPL-ICI2 can operate independently with a detection sensitivity capable of detecting all but the thinnest cirrus clouds. The compact JPL-ICI2 system, which utilizes the IR window, can provide high-temporal-resolution cloud measurements with no difference in day/night sensitivity during periods of adverse weather.

With adequate data, including the enclosure internal temperature (currently estimated as the camera temperature) and external temperature, this correction can be applied in real time. This allows the JPL-ICI2 system to run without support from the MSU-ICI2, which is run in a weather-hardened enclosure, and to achieve continuous observation and classification of cloud cover with only a small reduction of sensitivity (clouds with optical depth greater than 0.25). Future improvements in the camera and calibration procedures and the additional measurement of enclosure and window temperatures should continue to improve the minimum level of cloud sensitivity.

These experiments were performed over a range of internal enclosure temperatures (from 10° to 32°C) and external weather conditions (from 6° to 21°C) with a range of internal-to-external temperature differences (from 2° to 12°C). Currently, the JPL-ICI2 cloud imaging system is deployed at the Jet Propulsion Laboratory Table Mountain Facility, California, and data from this deployment will allow the assessment of this algorithm

Uncorrected Difference   Corrected Difference

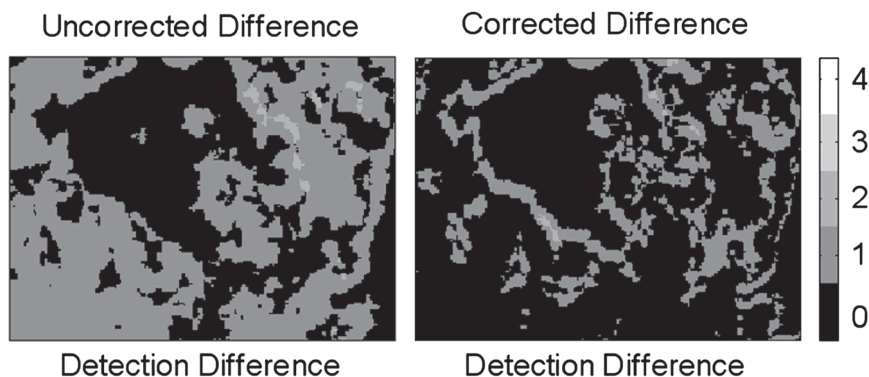Detection Difference   Detection Difference

FIG. 9. Difference of cloud detection images from two cloud imagers for 1906 MDT 2 Oct 2007 (left) before and (right) after correction. The grayscale bar indicates the magnitude of the error in terms of the number of cloud classification bins from Table 1. The IR window correction greatly reduces the differences to mostly one cloud classification bin at the cloud edges because of slight misalignments between the imagers and small calibration differences.

under a wide variety of weather conditions. Data from this deployment will also help determine if the window correction is sufficiently stable to allow a calibrated LWIR camera to operate inside a weather-hardened enclosure over an extended period of time.

REFERENCES

Anderson, G. P., and Coauthors, 1999: MODTRAN4: Radiative transfer modeling for remote sensing. *Optics in Atmospheric Propagation and Adaptive Systems III,* A. Kohnle and J. D. Gonglewski, Eds., International Society for Optical Engineering (SPIE Proceedings, Vol. 3866), 2–10.

Bevington, P. R., 1969: *Data Reduction and Error Analysis for the Physical Sciences.* McGraw-Hill, 323 pp.

Eloranta, E. W., J. P. Garcia, I. A. Razenkov, T. Uttal, and M. Shupe, 2008: Cloud fraction statistics derived from 2-years of high spectral resolution LIDAR data acquired at Eureka, Canada. *Proc. 24th Int. Laser Radar Conf.,* Boulder, CO, NCAR and NOAA, 555–558.

Han, Y., J. A. Shaw, J. H. Churnside, P. D. Brown, and S. A. Clough, 1997: Infrared spectral radiance measurements in the tropical Pacific atmosphere. *J. Geophys. Res.,* **102,** 4353–4356.

Jessup, A. T., and R. Branch, 2008: Integrated ocean skin and bulk temperature measurements using the Calibrated Infrared In situ Measurement System (CIRIMS) and through-hull ports. *J. Atmos. Oceanic Technol.,* **25,** 579–597.

——, R. A. Fogelberg, and P. J. Minnett, 2002: Autonomous shipboard infrared radiometer system for in situ validation of satellite SST. *Earth Observing Systems VII,* W. L. Barnes, Ed., International Society for Optical Engineering (SPIE Proceedings, Vol. 4814), 222–229.

Knuteson, R. O., and Coauthors, 2004: Atmospheric emitted radiance interferometer. Part I: Instrument design. *J. Atmos. Oceanic Technol.,* **21,** 1763–1776.

Minnett, P. J., R. O. Knuteson, F. A. Best, B. J. Osborne, J. A. Hanafin, and O. B. Brown, 2001: The Marine-Atmospheric Emitted Radiance Interferometer: A high-accuracy, seagoing infrared spectroradiometer. *J. Atmos. Oceanic Technol.,* **18,** 994–1013.

Nugent, P. W., 2008: Wide-angle infrared cloud imager for cloud cover statistics. M. S. Thesis, Dept. of Electrical Engineering, Montana State University, 163 pp. [Available online at http://etd.lib.montana.edu/etd/2008/nugent/NugentP0508.pdf.]

——, J. A. Shaw, and S. Piazzolla, 2009: Infrared cloud imaging in support of Earth-space optical communication. *Opt. Express,* **17,** 7862–7877.

Sassen, K., and G. G. Mace, 2002: Ground based remote sensing of cirrus clouds. *Cirrus,* D. K. Lynch et al., Eds., Oxford University Press, 188–192.

Shaw, J. A., P. W. Nugent, N. J. Pust, and B. Thurairajah, 2005: Radiometric cloud imaging with an uncooled microbolometer thermal infrared camera. *Opt. Express,* **13,** 5807–5817.

Thurairajah, B., and J. A. Shaw, 2005: Cloud statistics measured with the Infrared Cloud Imager (ICI). *IEEE Trans. Geosci. Remote Sens.,* **43,** 2000–2007.